The Astrophysical Journal, 857:80 (11pp), 2018 April 20 https://doi.org/10.3847/1538-4357/aab669

Discovery of a New Classical Nova Shell Around a Nova-like Cataclysmic Variable

Martín A. Guerrero[1], Laurence Sabin[2], Gagik Tovmassian[2], Edgar Santamaría[3,4], Raul Michel[2], Gerardo Ramos-Larios[4], Alexandre Alarie[2], Christophe Morisset[2], Luis C. Bermúdez Bustamante[2], Chantal P. González[2], and Nicholas J. Wright[5]

[1] Instituto de Astrofísica de Andalucía, IAA-CSIC, Glorieta de la Astronomía s/n, E-18008 Granada, Spain; mar@iaa.es
[2] Instituto de Astronomía, Universidad Nacional Autónoma de México, Apdo. Postal 877, C.P. 22860, Ensenada, B.C., Mexico
[3] Centro Universitario de Ciencias Exactas e Ingenierías, CUCEI, Universidad de Guadalajara, Av. Revolución 1500, C.P. 44860, Guadalajara, Jalisco, Mexico
[4] Instituto de Astronomía y Meteorología, Dpto. de Física, CUCEI, Universidad de Guadalajara, Av. Vallarta 2602, C.P. 44130, Guadalajara, Jalisco, Mexico
[5] Astrophysics Group, Keele University, Keele ST5 5BG, UK
Received 2017 August 17; revised 2018 March 9; accepted 2018 March 11; published 2018 April 17

Abstract

The morphology and optical spectrum of IPHASX J210204.7+471015, a nebula classified as a possible planetary nebula are, however, strikingly similar to those of AT Cnc, a classical nova shell around a dwarf nova. To investigate its true nature, we have obtained high-resolution narrowband [O III] and [N II] images and deep optical spectra. The nebula shows an arc of [N II]-bright knots notably enriched in nitrogen, while an [O III]-bright bow shock is progressing throughout the ISM. Diagnostic line ratios indicate that shocks are associated with the arc and bow shock. The central star of this nebula has been identified by its photometric variability. Time-resolved photometric and spectroscopic data of this source reveal a period of 4.26 hr, which is attributed to a binary system. The optical spectrum is notably similar to that of RW Sex, a cataclysmic variable star (CV) of the UX UMa nova-like (NL) type. Based on these results, we propose that IPHASX J210204.7 + 471015 is a classical nova shell observed around a CV-NL system in quiescence.

Key words: ISM: jets and outflows – novae, cataclysmic variables – stars: individual (IPHAS J210205.83 +474018.0)

1. Introduction

Many Galactic emission-line surveys have been completed in recent years. Most of them have focused on the Hα line (e.g., the Southern Hα Sky Survey Atlas SHASSA, the INT Photometric Hα Survey IPHAS, the SuperCOSMOS Hα Survey SHS, and the VST Photometric Hα Survey of the Southern Galactic Plane and Bulge VPHAS+; Gaustad et al. 2001; Drew et al. 2005, 2014; Parker et al. 2005), but also on molecular emission lines of H_2 (e.g., the UKIRT Widefield Infrared Survey for H_2 UWISH; Froebrich et al. 2011). These surveys offer the possibility of detecting different types of diffuse emission sources and emitting-line stars (Witham et al. 2008; Froebrich et al. 2015). Among the former, many new planetary nebulae (PNe; Viironen et al. 2009; Sabin et al. 2014), Wolf–Rayet nebulae (Gvaramadze et al. 2010; Stock & Barlow 2010), novae (Wesson et al. 2008; Sahman et al. 2015), nebulae ejected from massive evolved stars (Wright et al. 2014), and supernova remnants (Sabin et al. 2013) candidates have been uncovered, whereas among the latter, many emission-line star candidates, such as chromospherically active T-Tauri and late-type stars (Barentsen et al. 2011; Kalari et al. 2015); Be stars (Raddi et al. 2013); massive early stars (Mohr-Smith et al. 2015); interacting binaries and cataclysmic variables (Pretorius & Knigge 2008); and symbiotic stars (Corradi et al. 2010) have been reported.

Follow-up spectroscopic observations are in most cases required to verify the nature of these sources. This has been the case of Galactic PNe, whose number has increased notoriously (see the compilations in the Macquarie and Hong-Kong/Australian Astronomical Observatory/Strasbourg Observatory Hα Planetary Nebula MASH PN and HASH PN databases; Parker et al. 2006, 2016). In an attempt to confirm the nature of IPHAS PN candidates, Sabin et al. (2014) has carried out a spectroscopic follow-up of IPHAS sources and identified 159 new true, likely, and possible PNe. Among these sources, the nebula IPHASX J210204.7+471015 (also known as PN G088.0+00.4, hereafter J210204), classified as a possible PN, has a very peculiar morphology and spectral properties. The IPHAS Hα+[N II] image reveals an arc-like of emission that is reminiscent of the morphology seen in the nova shell around the dwarf nova AT Cnc (Shara et al. 2012). Moreover, the optical spectrum reveals a lack of Balmer lines, which is not typical for PNe, but is frequently seen in nova shells (Tarasova 2014). The morphology and spectral properties of J210204 cast doubts on its PN nature and rather point to a nova event at its origin.

Nebular shells around novae are scarce (Sahman et al. 2015), but they reveal interesting information to date the nova event, to study the details of the nova ejection, and to investigate its interaction with the circumstellar (CSM) and interstellar (ISM) media. This has motivated us to undertake an observational project to investigate the real nature of J210204. Deep narrowband optical images have been used to study its morphology in detail, whereas deep optical spectra of its nebular emission have been obtained to assess its spectral properties. The central star has been identified, and photometric and spectroscopic monitoring have been used to study its variability. These observations are described in Section 2. The nebular morphology, spectral properties, and the stellar properties are presented in Section 3. The nature and evolutionary status of J210204 are discussed in Section 4.

2. Observations

2.1. NOT Optical Imaging

Narrowband optical images in the [O III] λ5007 and [N II] λ6583 lines were obtained on 2017 May 27 and 28 using the Andalucia Faint Object Spectrograph and Camera (ALFOSC)

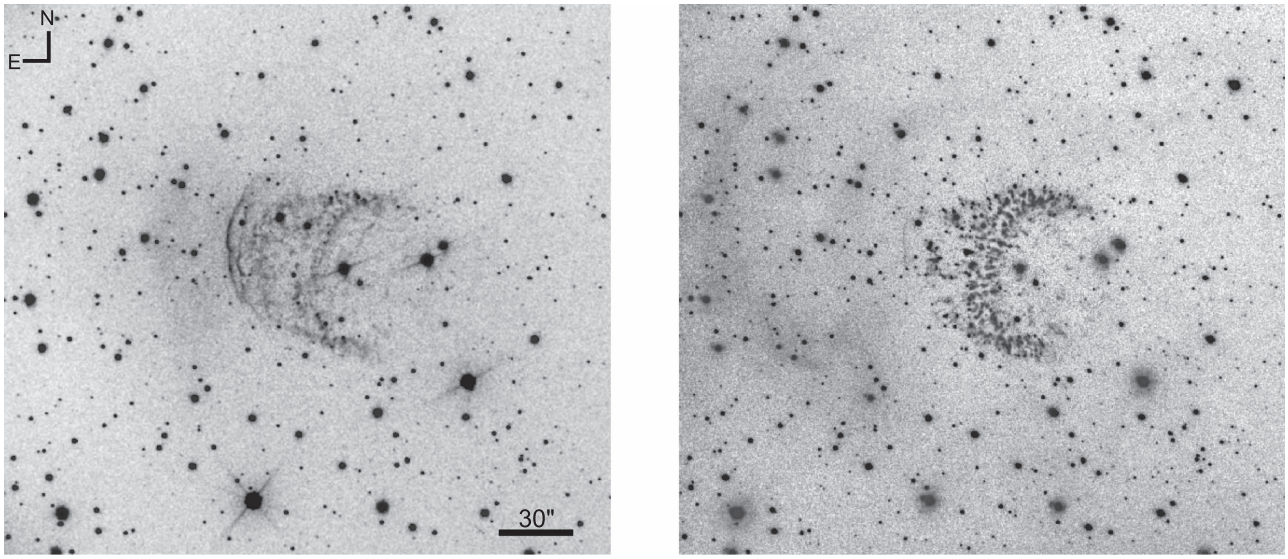

Figure 1. NOT ALFOSC [O III] (left panel) and [N II] (right panel) narrowband images of J210204.

mounted at the Cassegrain focus of the 2.5 m Nordic Optical Telescope (NOT) at the Observatorio de El Roque de los Muchachos (ORM, La Palma, Spain). The images were obtained using the NOT #90 [O III] 501_3 and the Observatorio de Sierra Nevada [N II] #E16 narrowband filters with central wavelengths and FWHM of 5007 Å (30 Å) and 6584 Å (10 Å). The EEV 231–42 2K×2K CCD was used, providing a pixel scale of 0.″211 and a field of view (FoV) of 7.′0.

Three 1200 s and two 900 s were secured in the [O III] and [N II] filters, respectively, to remove cosmic rays. The images were bias subtracted and flat-fielded using appropriate sky flat-field images, and then combined using IRAF[6] standard routines. The spatial resolution of the images as derived from stars in the FoV is 0.″7. The [O III] and [N II] images of J210204 are presented in Figure 1 together with a composite color picture in Figure 2.

2.2. SPM Photometric and Spectroscopic Monitoring

2.2.1. Photometry

The CCD camera Mexman mounted on the 0.84 m telescope of the Observatorio Astronómico Nacional at San Pedro Mártir (OAN SPM, Mexico) was used to perform time-resolved photometry of the stellar field around J210204. The E2V-4240 CCD ("Spectral Instrument 1") detector was used. The detector has 2048 × 2048 pixels with size 13.5 μm, but a 2 × 2 binning was used during the observations. The resulting plate scale and FoV were 0.″434 and 7.′4 × 7.′4, respectively. Alternating *BVRI* observations were taken with exposure times of 60, 40, 20, and 15–20 s, respectively. A preliminary inspection of these data sets reveals the variability of the bright star at the geometrical center of J210204 (see Figure 2), which was then selected as the most likely progenitor of this nebula. The coordinates of this star, as implied from the astrometric measurements and corrections for all IPHAS objects (Barentsen et al. 2014), are $\alpha_{J2000} = 21^h02^m05^s.82$, $\delta_{J2000} = +47°10'18.''00$. The positional error of this source, as referenced to the 2MASS data catalog, is 0.″06. For consistency, we will keep the designated IPHAS name for the central star, which hence is IPHAS J210205.83+471018.0.

The log of the photometric observations can be found in Table 1. Data were reduced using standard IRAF aperture photometry routines. In preparation for this work, the same field was observed on 2016 August 26 and calibrated with Landolt standard stars. The star 2MASS J21020346+4707113, with measured magnitudes of $B = 14.04$, $V = 13.42$, $R = 13.01$, and $I = 12.57$, was found to be the best reference star, as it has the most similar colors to those of the target star.

2.2.2. Spectroscopy

Time-resolved spectroscopic data were obtained with the Boller & Chivens spectrograph installed on the OAN SPM 2.1 m telescope. We obtained a series of spectra using the 1200 l mm^{-1} grating, which provides a spectral dispersion of 1.16 Å pix^{-1}. Coupled with the slit width of 1.″5, this results in a spectral resolution ≃3.2 Å, which is suitable to study radial velocity (RV) variations of ≃30 km s^{-1}. The 600 l mm^{-1} grating was also used to obtain low-resolution spectra covering a wide range of wavelengths in the optical domain. The CuArNe lamp was employed to obtain wavelength calibration arcs. The spectrophotometric standards Feige 110, BD+28° 4211 and G 191B2B were observed each night to allow the flux calibration of the source spectra. Standard procedures, including bias and flat-field correction, cosmic ray removal, and wavelength and flux calibration were applied using IRAF routines. Table 2 presents the log of these spectrophotometric observations.

2.3. GTC Optical Spectra

Intermediate-resolution long-slit spectroscopic observations were carried out with the Optical System for Imaging and low-Intermediate-Resolution Integrated Spectroscopy (OSIRIS) at the 10.4 m GTC telescope of the ORM on 2016 June 10 and 2016 August 28. OSIRIS was used in standard mode, with two Marconi CCD42-82 (2048 × 4096 pixels) detectors. The

[6] IRAF is distributed by the National Optical Astronomy Observatories, which are operated by the Association of Universities for Research in Astronomy, Inc., under a cooperative agreement with the National Science Foundation.

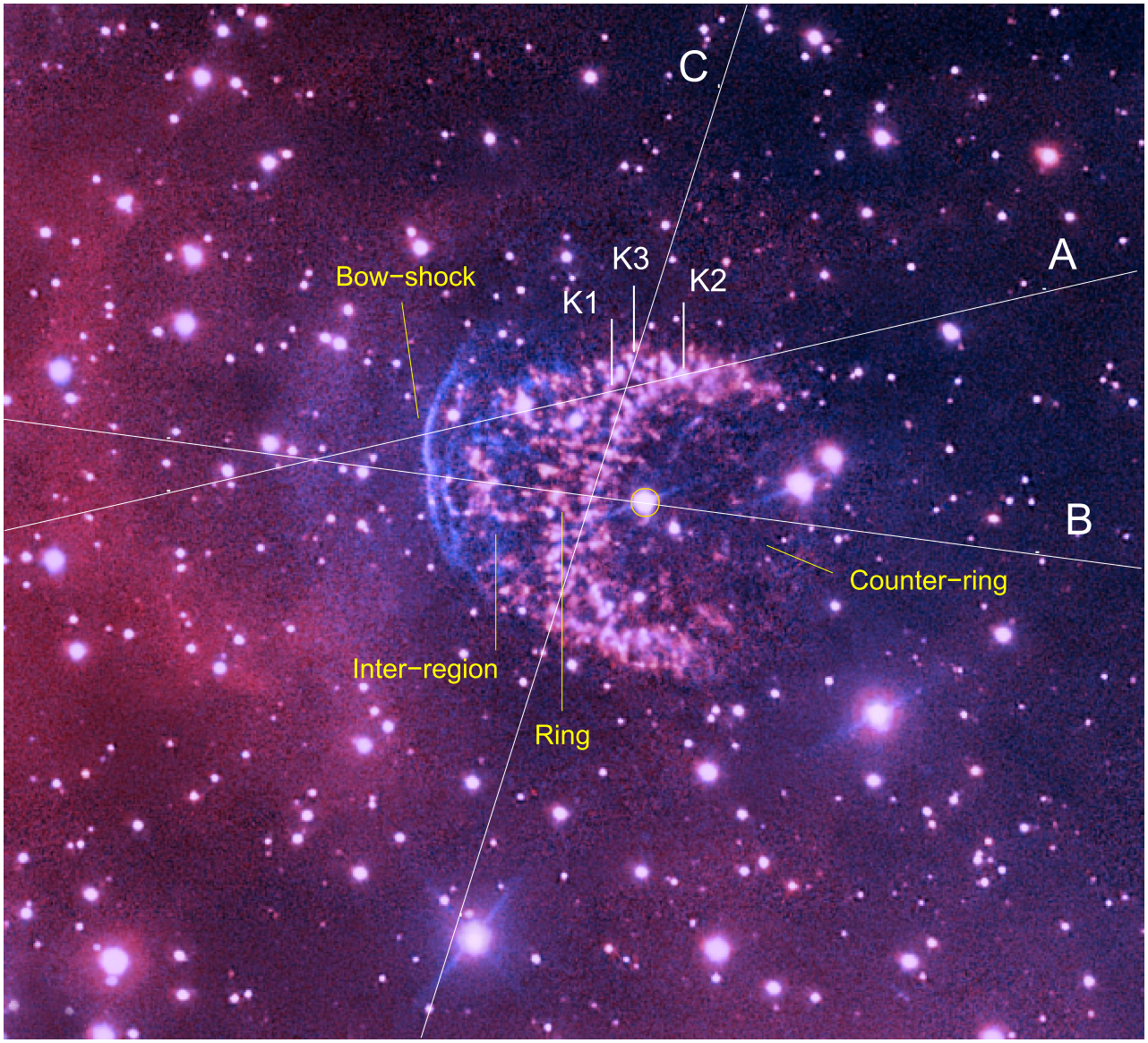

Figure 2. NOT ALFOSC color-composite picture of J210204 using the [N II] (red) and [O III] (blue) narrowband images presented in Figure 1. The positions of the GTC OSIRIS long-slits are marked on the picture. The different morphological components whose spectra are shown in Figure 3 are labeled, as well as the location of the three individual knots K1, K2, and K3, whose spectra are shown in Figure 4. The central star is encircled.

Table 1
Photometric Observing Log

Date	HJD Start Time +2457600 (day)	HJD End Time +2457000 (day)	Coverage (hr)
2016 Aug 31	31.795520	31.971839	4.2
2016 Sep 01	32.808253	32.971219	3.9
2016 Sep 02	33.817217	33.965623	3.6
2016 Sep 29	60.688186	60.815632	3.1
2016 Oct 01	62.661248	62.876114	5.2
2016 Oct 02	63.693037	63.836978	3.4
2016 Oct 03	64.665781	64.821321	3.7
2016 Oct 05	66.622653	66.734812	2.7

2×2 on-chip binning resulted in a spatial scale of $0\farcs254$ pix^{-1}. The R1000B and R1000R grisms were used to acquire spectra in the blue and red regions of the optical spectrum, respectively, covering the spectral range from 3630 to 10000 Å. Their spectral dispersions are 2.12 Å pix^{-1} and 2.62 Å pix^{-1}, respectively. A slit width of $1\farcs2$ was used, resulting in a spectral resolution $\simeq$9 Å.

The slit, with length $7\farcm4$, was placed along different position angles (PA) to cover distinct morphological components of J210204. The details of the observations are listed in Table 3, including the slit keyword (as shown in Figure 2), the grism, PA, offset from the central star, and number of exposures and integration time at each slit position. These data sets are also described in Table 2.

The data reduction was carried out using standard IRAF routines. Hg–Ar, Ne, and Xe arcs were used for wavelength calibration. The spectrophotometric standards G191-B2B and Feige 110 were used for flux calibration. The seeing, as determined from the FWHM of the continuum of field stars covered by the slit, was $\simeq1\farcs0$.

Table 2
Spectroscopic Observing Log

Date	HJD +2450000 (day)	Telescope	Instrument	Spectral Coverage (Å)	Spectral Dispersion (Å pix^{-1})	Number of Exposures	Exposure Time (s)	Time Coverage (m)
2016 Aug 10	7610	OAN 2.1 m	B&Ch	4400–5620	0.59	5	1200	100
2016 Aug 11	7611	OAN 2.1 m	B&Ch	4400–5620	0.59	5	1200	100
2016 Aug 12	7612	OAN 2.1 m	B&Ch	4400–5620	0.59	9	1200	200
2016 Aug 14	7614	OAN 2.1 m	B&Ch	4400–5620	0.59	6	1200	120
2016 Aug 15	7615	OAN 2.1 m	B&Ch	4400–5620	0.59	6	1200	120
2016 Aug 28	7628	GTC	OSIRIS	3650–7820	2.07	8	340	75
2016 Aug 28	7628	GTC	OSIRIS	5110–10340	2.59	8	300	75
2016 Sep 25	7656	OAN 2.1 m	B&Ch	4150–6510	1.16	9	900	140
2016 Sep 26	7657	OAN 2.1 m	B&Ch	4350–6710	1.16	15	900	230

Table 3
Details of the GTC OSIRIS Observations

Position	Grism	PA (°)	Offset (″)	N_{exp}	t_{exp} (s)
A	R1000B	103	24.6	2	738
A	R1000R	103	24.6	2	600
B	R1000B	83.5	0	8	340
B	R1000R	83.5	0	8	300
C	R1000B	164	12.7	2	738
C	R1000R	164	12.7	2	600

3. Data Analysis

3.1. The Nebula

3.1.1. Morphology

The most noticeable structure revealed by the narrowband images is a [N II]-dominated arc-like feature (Figures 1-right and 2). It consists of a myriad of knots distributed along two parallel strings that interweave at their tips. Many of those knots have a cometary morphology, with tails pointing outwards. A few knots also trace an eastern counterpart of the arc, but they are much fainter and sparse. The western double-arc feature is also detected in [O III], but the emission in this line is much smoother (Figure 1, left). We will refer to these two regions as the "ring" and the "counter ring," respectively, as marked in Figure 2.

There is an additional string of knots west of the ring, whose emission is similarly bright in the [N II] and [O III] emission lines. It must be noted, however, that the [N II] emission from this third arc arises from a sparse ensemble of discrete knots, whereas the [O III] emission does from a smooth arc. We will refer to this feature as the "inter-region" (Figure 2).

There is another arc of emission external to the previous ones. This arc is notably bright in [O III] with very faint [N II] emission. Contrary to the previous morphological features described above, the emission from this double-arc structure is notably sharp. Its morphology is clearly reminiscent of a bow-shock structure, so we will refer to it as the "bow shock" (Figure 2).

Along with these main morphological components, there are two additional arcs of diffuse emission in front of the "bow-shock" structure: the first one detected both in [O III] and [N II] at $\simeq 1\farcm5$ from the central star (Figures 1 and 2), the second one detected only in [N II] at $\simeq 2\farcm0$ from the central star (Figures 1-right and 2). This second arc along the direction of the [O III] bow shock is confirmed in large-scale IPHAS Hα +[N II] images.

3.1.2. Spectral Properties

We have used the deep GTC OSIRIS observations to extract 1D spectra of the different morphological components of J210204. The spectra, shown in Figure 3, corresponds to the bow-shock structure, the ring of [N II]-bright knots, the inter-region, and the counter ring.

As expected, the spectrum of the bright ring is dominated by the [N II] $\lambda\lambda$6548,6584 emission lines. The auroral [N II] λ5755 emission line is also detected, as well as the [N I] λ5199 emission line. The [O III] $\lambda\lambda$4959,5007 lines and the [O II] λ3727 doublet are also detected, but they are much fainter than the [N II] emission lines. Weak emission from the [S II] $\lambda\lambda$6717,6731 doublet is also detected. The Balmer lines are very weak and no helium lines are detected.

We note that the spectrum of different knots may vary significantly among them. We have selected three individual knots, marked in Figure 2 as K1, K2, and K3, to illustrate these variations. The spectra of these knots are shown in Figure 4. Knot K1 has the lowest [O III]/[N II] and [O II]/[N II] line ratios. Knots K2 and K3 have [O III]/[N II] line ratios typical of the ring, ∼0.3, but the [O II]/[N II] line ratios differ notably, from ∼0.5 in K2 to ∼0.2 in K3.

The spectrum of the counter ring looks very similar to that of the ring, although it is much fainter. On the contrary, the spectrum of the bow-shock feature is dominated by the [O III] $\lambda\lambda$5007,4959 emission lines. Hα emission is present, as well as Hβ. Indeed, Hα emission is brighter than the [N II] emission. Actually, owing to the presence of large-scale diffuse Hβ and Hα emissions, which make difficult the subtraction of the background emission, this is the only region where the detection of the Balmer lines are reliable.

Finally, the intensity of the [N II] λ6584 and [O III] λ5007 emission lines is very similar in the inter-region, i.e., their ratio shows an averaged behavior between those of the bow shock and the ring spectra. The Hα line is detected, but the intensity of the Hβ line is rather unreliable.

Table 4 shows the emission-line fluxes measured for the different regions of J210204. The fluxes of the [N II] $\lambda\lambda$6548,6584 and [O III] $\lambda\lambda$5007,4959 emission lines can be considered to be reliable within a few percent, except for the [O III] λ5007 emission line in the counter-ring region. The fluxes of the Hα emission line in the bow-shock spectra and the [O II] λ3727 doublet and [N II] λ5755 and [N I] λ5199 emission lines in the ring spectrum are also reliable.

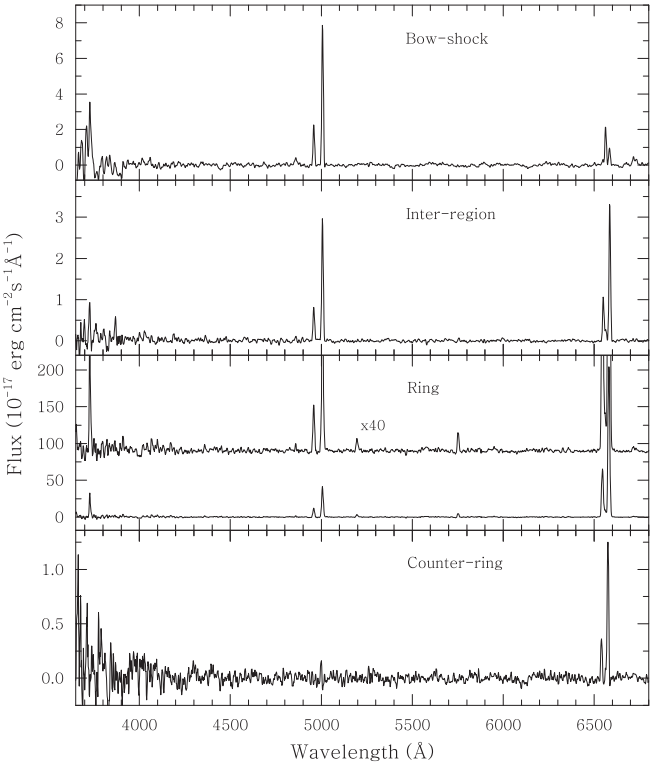

Figure 3. GTC OSIRIS 1D spectra of the different nebular components of J210204. The spectrum of the brightest region, the "Ring," is plotted at two different scales to show both the bright and faint emission lines.

We have used the Hα to Hβ ratio in the bow-shock region to derive a logarithmic extinction of 0.73. This correction has been applied to all regions. The relative intensities in Table 5 have been referred to that of Hβ equal to 1, but for the region of the counter ring, where the Balmer lines are not detected. In this region, the relative intensities of the [N II] and [O III] lines have been referred to that of the [N II] λ6584 line in the ring.

3.1.3. Excitation and Chemical Abundances

The relative line intensities listed in Table 5 are revealing. The weak emission in the Hβ and Hα lines implies that all regions have mostly high line ratios of [S II]/Hα, [N II]/Hα, [O III]/Hβ, and/or [O II]/Hβ: wherever the [S II] lines are detected, the [S II]/Hα line ratio is larger than 0.25, and the ring has [O II]/Hβ and [N II]/Hα line ratios $\simeq$30 and $\simeq$25, respectively. The spectrum of the bow shock is remarkably different from that of the ring, as it exhibits a low [N II]/Hα line ratio and emission in the He II λ4686 line. The line ratios detected in the different regions of J210204 discard a photoionization excitation, but they rather suggest that line emission is mostly excited by shocks (Hartigan et al. 1987).

The MAPPINGS 5.13 code (Sutherland & Dopita 2017) has been used to investigate key line ratios detected in the bow shock, inter-region, and ring to assess the properties of these shocks and the chemical abundances of the emitting material. Unfortunately, the available emission-line ratios are insufficient to fit simultaneously all parameters that critically determine the plasma emitting properties, mostly the shock velocity, chemical abundances, pre-ionization state of the gas, age of the shock, pre-shock density, and to a minor extent, the magnetic field.

As for the bow shock, a set of models was built using MAPPINGS 5.13 and its line ratio predictions compared with

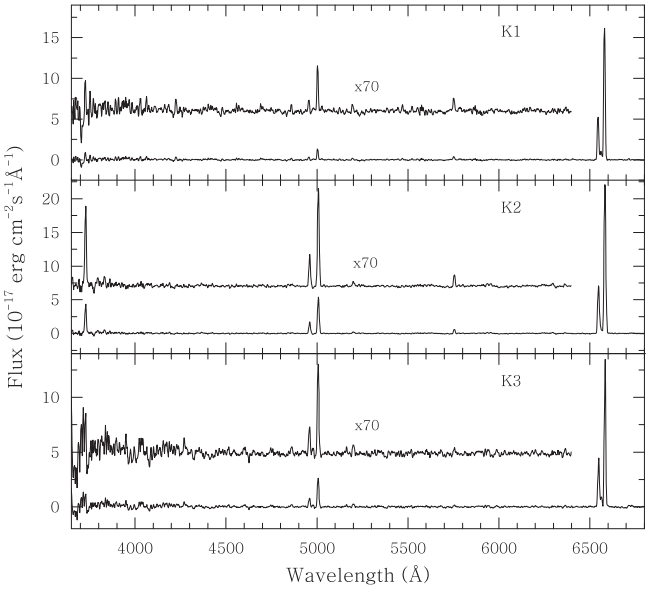

Figure 4. GTC OSIRIS 1D spectra of three selected knots of J210204 as marked in Figure 2. The spectra are shown at two different scales to highlight both the bright and faint emission lines.

those listed in Table 5. As the shocked gas is expected to be dominated by ISM material, its chemical abundances have been assumed to be solar (Asplund et al. 2009), and the pre-shock density and magnetic field have been adopted to be 5 cm^{-3} and 1 μG, respectively. The MAPPINGS models show that complete shocks lead to very low values of the [O III]/Hβ line ratios, indicating that the shock is incomplete, i.e., the shock has not had enough time to fully recombine and cool down yet. The predicted time evolution of some line ratios for a shock velocity of 150 km s^{-1} and the observed values are shown in Figure 5. The He II/Hβ, [O II]/Hβ, [O III]/Hβ, and [N II]/Hβ line ratios are reproduced at times varying between 200 and 500 years. Line ratios vary on a first-order linearly with the elemental abundances, making everything fit at an age $\sim$350 year if the oxygen abundances were reduced by a factor of three. We note, however, the strong degeneracy between age, shock velocity, and abundances, and the obvious simplicity of the model, which does not account for geometrical effects that superpose shocks of differing properties along the line of sight.

As for the ring and inter-region, the significant [N II]/[O II] line ratio variations between the ring (2.8) and inter-region (0.8) suggest the chemical enrichment of the material at the ring. The variations of the [N II]/[O II] line ratio have been simulated using also MAPPINGS for a range of shock velocities and O/H abundances, adopting this time a pre-shock density of 1000 cm^{-3}, consistent with the nova CSM material, and assuming the shock has had enough time to become complete. The results, plotted in Figure 6, are shown for solar N/O ratios, but the [N II]/[O II] line ratio can be scaled with the N/O ratio. This plot reveals that for shock velocities above 200 km s^{-1}, the [N II]/[O II] line ratio can be used as a diagnostic of the O/H abundances and N/O abundances ratio. The high [N II]/[O II] line ratio of the ring can only be interpreted with extremely high over-solar abundances (O/H $> 4 \times$(O/H)$_\odot$) or over-solar N/O ratios (N/O $\simeq 5\times$ (N/O)$_\odot$), or both of them, whereas the inter-region shows O/H abundances or N/O abundances ratio

Table 4
Emission-line Flux Measured in Different Regions of J210204

Line ID	Bow Shock	Inter-region	Ring	Counter Ring (10^{-16} erg cm^{-2} s^{-1})	Knot #1	Knot #2	Knot #3
[O II] 3727	4.16	1.62	30.9	⋯	1.34	4.30	0.93
He II 4686	0.20	⋯	⋯	⋯	⋯	⋯	⋯
Hβ	0.47	0.052	1.55	⋯	0.17	0.08	0.25
[O III] 4959	2.53	0.93	13.8	⋯	0.47	1.83	0.83
[O III] 5007	8.82	3.24	4.66	0.19	1.22	5.97	2.76
[N I] 5199	⋯	⋯	3.66	⋯	0.16	0.30	0.26
[N II] 5755	⋯	⋯	5.09	⋯	0.43	0.72	0.14
[N II] 6548	0.31	1.12	81.2	0.39	6.10	8.33	4.53
Hα	2.35	0.27	10.3	⋯	1.19	0.65	0.91
[N II] 6584	1.05	3.55	254	1.33	18.1	26.4	13.8
[S II] 6716	0.52	0.044	1.64	⋯	0.18	⋯	⋯
[S II] 6731	0.35	0.035	1.03	⋯	⋯	⋯	⋯

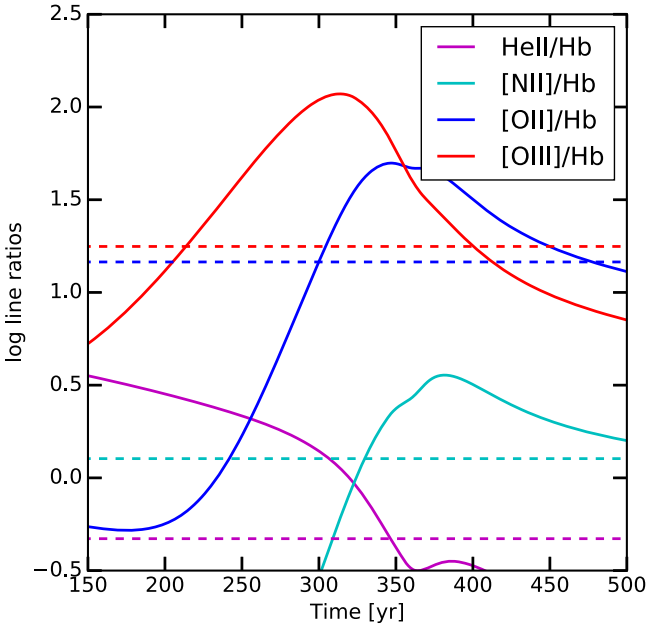

Figure 5. Time evolution of different line ratios for MAPPINGS simulations of an incomplete shock at a shock velocity 150 km s^{-1}, pre-shock density 5 cm^{-3}, and solar abundances as suitable for the bow shock.

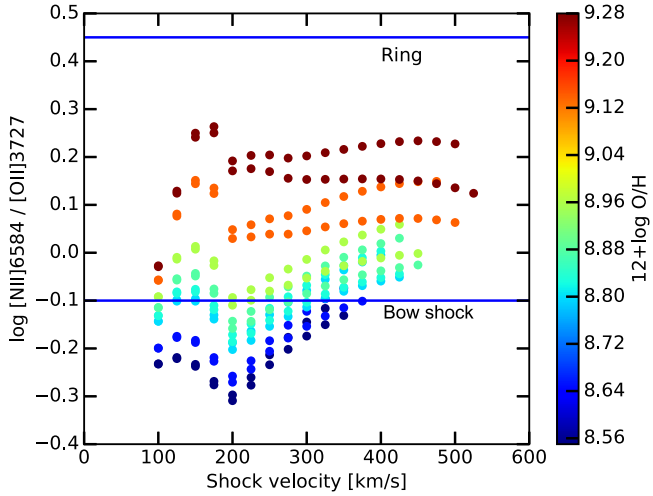

Figure 6. Variation of the [N II]/[O II] line ratios for MAPPINGS simulations of a complete shock vs. the shock velocity and O/H abundances for a pre-shock density 1000 cm^{-3}, solar N/O abundances ratio, and magnetic field of 1 and 5 μG. The horizontal lines mark the [N II] λ6584[O II] λ3727 line ratios of the ring and bow shock.

slightly over-solar. The large variations in the [N II]/[O II] line ratio among discrete knots in the ring can be similarly interpreted as evidence of large variations in their metallicity.

3.2. The Central Star

3.2.1. Spectral Properties

The normalized spectrum of the central star of J210204 presented in Figure 7 reveals prominent broad Balmer hydrogen absorption lines with embedded central emission peaks. Neutral helium lines are also observed as a combination of wide absorption and narrow emission. Strong NaD and a set of Fraunhofer lines are also detected in absorption in this spectrum, while Ca II and a blend of C III and fluorescent N III lines at 4640–50 Å are clearly seen in emission. The most prominent lines are marked with different colors in Figure 7.

3.2.2. Photometric Variability

The measured mean and 1σ deviation magnitudes derived from the photometric data obtained during the two main observing runs are 16.416 ± 0.009 mag in the *B*-band, 15.805 ± 0.009 mag in the *V*-band, 15.373 ± 0.012 mag in the *R*-band, and 14.856 ± 0.013 mag in the *I*-band. The inspection of the light curves reveals notable fluctuations. The discrete Fourier transform (DFT) based program PERIOD04 (Lenz & Breger 2005) was used to search for possible periodicities in the photometric data. The best results showing the lower dispersion are obtained in the *R*-band, for which a frequency $f_R = 5.628 \pm 0.011$ day^{-1} is found as revealed by the main peak in the power spectrum (the dotted gray line in the right panel of Figure 8). One-day aliases are strong, given the observational strategy; indeed, the power spectrum corresponding to the *I*-band actually peaks at 6.63 day^{-1}, i.e., $f_I = f_R + 1$. There is also a number of noticeable secondary peaks, resulting from the significant noise level in the power spectra induced by the low-resolution of the photometric data

Table 5
Dereddened Relative Intensity of the Emission Lines in J210204

Line ID	Bow Shock	Inter-region	Ring	Counter Ring	Knot #1	Knot #2	Knot #3
[O II] 3727	14.6 ± 5.6	51 ± 13	32.9 ± 1.6	⋯	13.5 ± 3.5	95 ± 5	0.20 ± 0.08
He II 4686	0.47 ± 0.23	⋯	⋯	⋯	⋯	⋯	⋯
Hβ	1.00 ± 0.22	1.0 ± 1.0	1.00 ± 0.18	⋯	1.00 ± 0.29	1.0 ± 0.8	1.00 ± 0.22
[O III] 4959	5.19 ± 0.20	17.0 ± 0.5	8.59 ± 0.20	⋯	2.65 ± 0.29	23.5 ± 0.7	3.22 ± 0.22
[O III] 5007	17.70 ± 0.25	58.4 ± 0.5	28.51 ± 0.26	22 ± 7	6.90 ± 0.35	75.4 ± 0.8	10.44 ± 0.25
[N I] 5199	⋯	⋯	2.07 ± 0.15	⋯	0.88 ± 0.29	3.5 ± 0.6	0.91 ± 0.19
[N II] 5755	⋯	⋯	2.37 ± 0.12	⋯	1.83 ± 0.22	6.9 ± 0.5	0.41 ± 0.12
[N II] 6548	0.37 ± 0.11	12.27 ± 0.27	30.16 ± 0.15	27.9 ± 2.4	20.87 ± 0.16	63.8 ± 0.4	10.40 ± 0.11
Hα	2.86 ± 0.13	3.00 ± 0.27	3.80 ± 0.08	⋯	4.05 ± 0.15	4.94 ± 0.32	2.09 ± 0.11
[N II] 6584	1.27 ± 0.13	38.46 ± 0.31	93.46 ± 0.27	93.5 ± 2.6	58.82 ± 0.22	200.0 ± 0.5	31.25 ± 0.16
[S II] 6716	0.61 ± 0.11	0.42 ± 0.19	0.58 ± 0.07	⋯	0.59 ± 0.14	⋯	⋯
[S II] 6731	0.41 ± 0.11	0.35 ± 0.23	0.36 ± 0.06	⋯	⋯	⋯	⋯

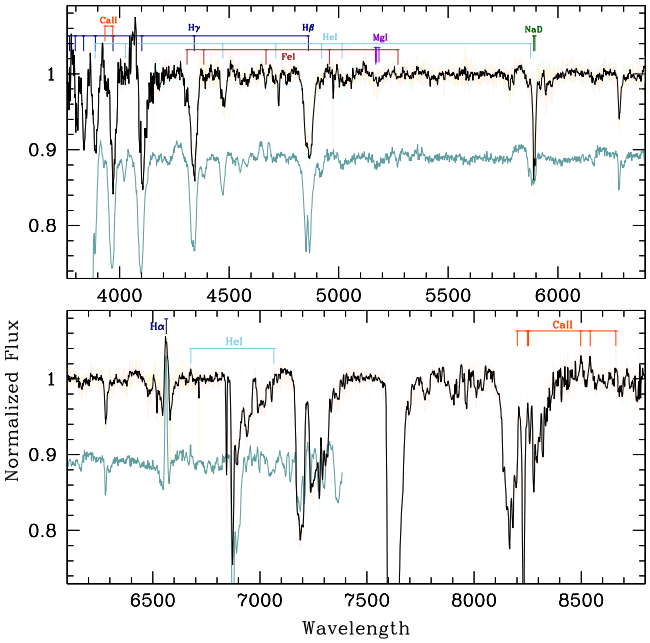

Figure 7. Normalized combined spectrum (SPM+GTC) of the central star of J210204 (black) compared with that of the UX UMa NL system RW Sex (green). The spectrum of RW Sex has been shifted by 0.11. Lines of interest are labeled.

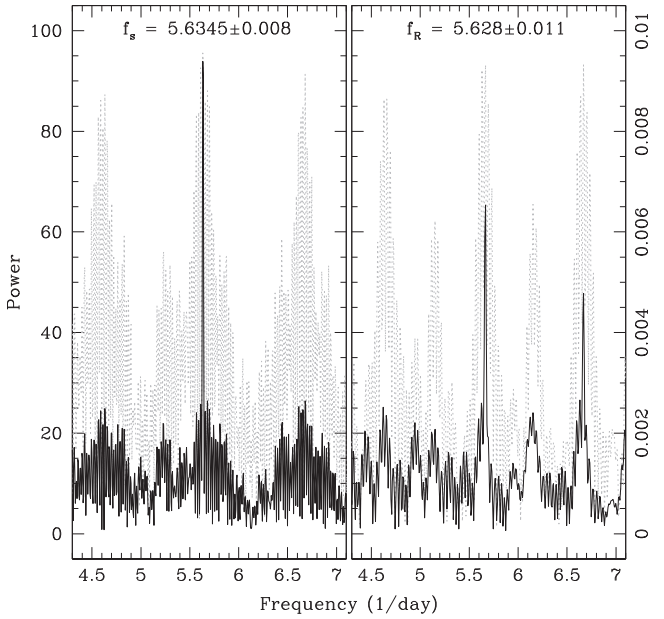

Figure 8. Power spectra of RV from the Hβ absorption (left) and *R*-band photometric (right) timeseries. The gray line in both panels is the power calculated by the DFT analysis, while the solid black line is the same after cleaning (see the text). The peak indicates a spectroscopic frequency $f_s = 5.6345$ day^{-1} and a photometric frequency $f_R = 5.628$ day^{-1}.

set. The convolution of the observed power with the spectral window helps to suppress aliases using a procedure appropriately called *Clean* (Roberts et al. 1987). The cleaned power spectrum of the *R*-band light curve (the solid black line in right panel of Figure 8) confirms the low-frequency peak. The frequency derived from the *R*-band implies a photometric period $P_{\rm ph} = 4.264 \pm 0.007$ hr. The folded light curve with this frequency show little variation in shape among the different photometric bands (Figure 9). The global change in magnitudes throughout the different bands is relatively small, ∼0.1 mag.

There is also a remarkable trend in the long-term light curve. The power spectrum reveals the presence of a peak at $f = 0.085$ day^{-1}, which would imply a cyclical variability with a period of 11.7 day, although we reckon that the length of the observing runs is not appropriate to investigate such a long-term variability. Another noteworthy peak is actually a one-day alias at a frequency 0.92 day^{-1} that corresponds to a period of 26.1 hr. The power strength shifts from one peak to the other depending on the photometric band.

3.2.3. Radial Velocity Variability

The photometric variability may be associated with RV variations. To investigate these, we have used the narrow-emission component of the Balmer Hα line and the Balmer Hβ absorption line (see Figure 10). The Hβ line is not symmetric and very wide, with a FWHM ≈ 40–50 Å and a full width at zero intensity (FWZI) up to ≈140 Å. In the absence of a clear understanding of the nature of different components that may form the Hβ line profile, we measured it using a single Gaussian. The analysis of the RV variations with PERIOD04 clearly shows periodic modulation, with a strong peak around a frequency of 5.6 day^{-1} (with its unavoidable one-day alias). In a similar way as for the photometric light curves, the uneven timeseries produces alias peaks in the power spectrum. These have been convolved with the spectral window to clean aliases.

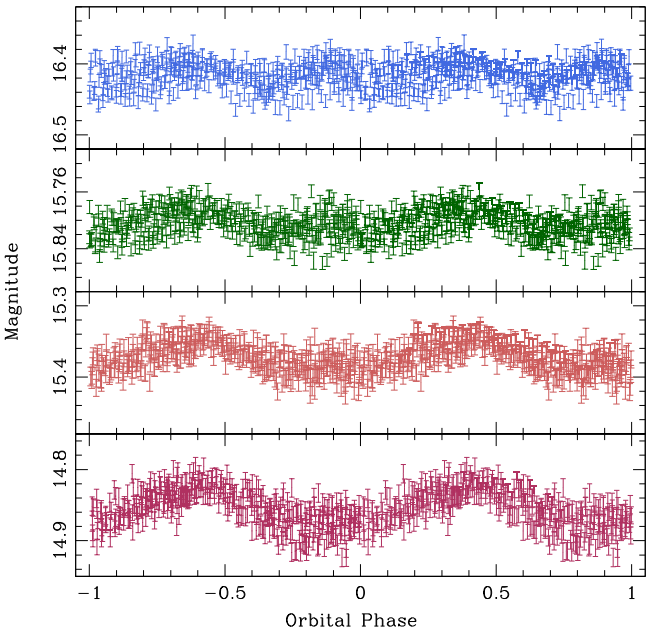

Figure 9. Magnitudes variations folded according to the photometric period of $P_{\rm ph} = 4.264$ hr for the *B*, *V*, *R*, and *I* bands from top to bottom, respectively.

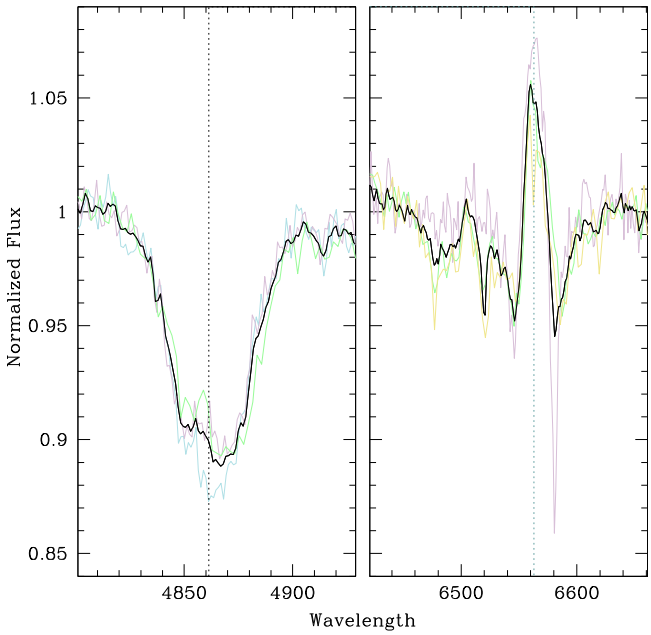

Figure 10. Hβ absorption (left) and Hα emission (right) profiles. The thin colored lines show profiles observed at different times, whereas the thick black line correspond to the averaged profiles. The dashed vertical lines mark the rest wavelength of both lines.

The raw and cleaned resulting power spectrum are shown in the left panel of Figure 8, where the cleaned power spectrum peak corresponds to a frequency $f_s = 5.635 \pm 0.008\,{\rm day}^{-1}$ (or to a period $P_s = 4.260 \pm 0.006$ hr). This value deviates from the period derived from the photometric data by ∼0.3 minutes, which is within the 3σ formal uncertainty. In the following, we will favor the period determined from spectroscopic observations, as this has been derived from a more complete timeseries distribution and the data analysis shows a more robust variability. Additional photometric and spectroscopic data are needed to improve the accuracy of the period determination to assess whether there is a real difference between the spectroscopic and the photometric period.

As for the Hα line, we measured only the dominant emission peak located close to the rest wavelength of the line. Even though this component looks single-peaked and narrow compared with the entire Hα complex, it actually splits into two components at certain orbital phases. We used the de-blending option in the IRAF procedure *splot* to fit two distinct Gaussian components to the line profile whenever they were present. The brightest component is basically seen throughout the whole orbital cycle, and it follows the RV curve deduced from Hβ, but with a much smaller RV amplitude. The RV of the narrower and fainter component, which is detected only in half of the orbital phases, varies in a near counterphase to the first component and to the wide absorption measured with Hβ.

Finally, a careful examination of the NaD doublet shows a faint component with variable RV in addition to the deep narrow absorption lines that can be attributed to the ISM and may be CSM. The variable component is in phase with the wide Hβ absorption.

4. On the Nature of IPHASX J210204.7+471015

4.1. The Central Star IPHAS J210205.83+471018.0

The optical spectrum of the central star of J210204 shows wide absorption lines of H I and He I with narrow-emission cores. These spectral features are distinctive of UX UMa nova-like (NL) systems (Dhillon 1996), a sub-class of non-magnetic cataclysmic variable stars (CVs). Indeed, the comparison of the optical spectrum of the central star of J210204 with that of the UX UMa system RW Sex (Beuermann et al. 1992, and references therein) obtained with the same settings at the same telescope (Hernández et al. 2017) show that both spectra are basically identical (Figure 7). Both stars show spectral lines mostly in absorption, which is consistent with a rather optically thick accretion disk in a NL, although sometimes it is difficult to discern them from similar set of lines produced by a K donor star. The main difference between the spectrum of RW Sex and that of J210204 central star is the presence of multiple emission peaks inside Balmer lines (Figure 10), a fact normally associated with a post-nova shell stage. Emission lines are limited to the notable Hα line, and to the high excitation lines of He II 4686 Å and a blend of C III and fluorescent N III at ≃4650 Å. This places the central star of J210204 on the upper part (or high state) in the disk surface density (Σ) versus disk temperature (T) plot (Mineshige & Osaki 1985; Cannizzo 1993), i.e., the locus of CV-NL objects, a sub-class of CVs characterized by high and stable mass-transfer rates ($\dot{M} \geqslant 10^{-9} M_\odot$ yr^{-1}) and a steady-state accretion disk (Meyer & Meyer-Hofmeister 1982). Accordingly, the brightness of NLs does not vary significantly around its mean level, in agreement with the small ∼0.1 mag variation found for J210204 (Figure 9).

The concordant periodic photometric and RV variations of the central star of J210204 reinforces the idea that it consists of a binary system in a nova, where the viewing aspect at different orbital phases of the system comprised by a compact source, an accretion disk around it, and a donor star would produce the observed periodic variations. The observed 4.26 hr period can be interpreted as the orbital period of the binary system. The short period is again consistent with a CV classification for this source. Otherwise, the long-term photometric period of 11.7 days,

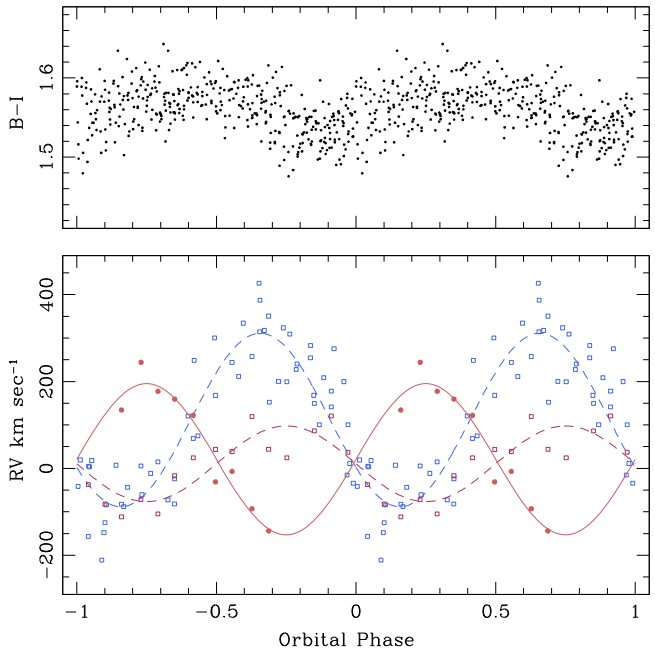

Figure 11. Photometric $B - I$ (top panel) and RV (bottom panel) variability folded with the spectroscopic phase. In the bottom panel, the red solid line and dots corresponds to the faint Hα component, the red dashed line and open symbols to the bright Hα component, and the blue dashed line and open symbols to the Hβ absorption.

although not well understood, is not exceptional in these systems (Yang et al. 2017) and may be caused by the precession of the accretion disk (de Miguel et al. 2016).

In the absence of eclipses, it is difficult to associate the different emission and absorption line components with the system constituents, but the varying amplitudes and phasing of these spectral line components, as seen in the bottom panel of Figure 11, can provide important clues about this system. The similarities of the central star of J210204 to other NLs (Hernández et al. 2017) makes us assume that the narrow faint Hα emission component (the red solid line and dots in the bottom panel of Figure 11) originates at the irradiated face of the donor star. The RV curve of this component thus reflects the motion of the secondary star. Consequently, we will assign the zero phase to the time $T_0 = 2457610.5154$, at which this RV curve crosses the systematic velocity line. When the RV plots are referred to this zero point and folded with the 4.26 hr spectroscopic period (the bottom panel of Figure 11), the emission of the faint Hα component apparently fades away and disappears between phases –0.3 and 0.2. This can be taken as a good evidence that this Hα emission component arises only from the side of the donor star facing the accretion disk that would be not visible to the observer in this phase interval. The sinusoidal fit to the Hα measurements indicates a RV semi-amplitude of $\sim$175 km s^{-1}. The secondary star velocity implies a high orbital inclination angle, although not high enough to produce eclipses in this system.

Meanwhile, the broad Hβ absorption probably originates in the optically thick accretion disk. This optically thick accretion disk would outshine the stellar components of the binary system so that no signature of the narrow absorption lines from the secondary star is visible. If the Hβ absorption line formed evenly in the entire accretion disk, then it would be expected its RV curve to be in phase with that of the narrow faint Hα emission component originating from the secondary star, as in the case of RW Sex (see Figure 6 in Beuermann et al. 1992). However, the orbital phasing of the Hβ absorption (the blue open squares and blue dashed line in the bottom panel of Figure 11) is not exactly in counterphase with the narrow faint Hα emission component (red solid line and dots in the bottom panel of Figure 11). The maximum positive velocity of the Hβ RV curve at $\phi = 0.65$, and its large amplitude indicate that the line emanates predominately from the co-rotating hot spot. At that orbital phase, the intrinsic velocity of the matter in the hot spot would be increased by the orbital velocity. This is not a novelty, as the asymmetry of the accretion disks of UX UMa systems has been noted before (e.g., Schlegel et al. 1983; Neustroev et al. 2011).

Finally, the bright Hα emission component (red open squares and dashed line in the bottom panel of Figure 11) can be attributed to an extended and low-velocity region located off the edge of the accretion disk and opposite to the hot spot, as for 1RXS J064434.5 + 334451 (Hernández et al. 2017). This interpretation is consistent with the observed photometric variations of the system, as shown in the upper panel of Figure 11, where the $B - I$ color curve folded with spectroscopy ephemeris is plotted. The maximum color difference is achieved at $\phi \simeq 0.4$, just prior to the inferior conjunction of the presumed late-type donor star. The amplitude of the photometric variations grows toward longer wavelengths, reaching 0.04-0.06 mag in the I-band (Figure 9). The light curves in red filters are not symmetric, but the $B - I$ color curve is, thus suggesting that color stays more or less constant with some blue light being obscured around $\phi = 0.9$. This might be evidence of the dark spot detected in the archetype UX UMa itself (see Figure 9 in Neustroev et al. 2011), but our spectrosopic data is not sufficient to conduct a similar tomographic analysis and confirm the evidence of such dark spot in the central star of J210204.

4.2. The Nebula IPHASX J210204.7+471015

The shell around this binary system bears a striking resemblance to the nova AT Cnc, particularly in the low-ionization [N II] emission line. The cometary morphology of many of the [N II] knots and the [O III] bow shock are highly indicative of a recent outburst event that is seen as a bow shock progressing through the ISM. Shock-sensitive line ratios are indeed suggestive of shocks (Hartigan et al. 1987). A detailed spatio-kinematical study of the different nebular components is underway (E. Santamaría et al. 2018, in preparation).

Novae are expected to produce noticeable amounts of CNO, as well as Ne, Mg, Al, and Si (e.g., José & Hernanz 1998), a theoretical expectation confirmed by spectroscopic observations of classical nova shells (Gehrz et al. 2014; Tarasova 2016). The chemical abundances of the different regions of J210204 cannot be derived in detail, but the [N II]/[O II] line ratios, in the assumption of complete shocks, imply a significant gradient in the abundances from the ring to the inter-region. The high N/O ratio of the ring, well above unity as typically found in novae (Nussbaumer et al. 1988), reveals pristine nova ejecta, whereas the inter-region displays chemical abundances closer to those of the ISM, as the nova ejecta expand and sweep up ISM material. Individual knots may show evidence of larger chemical enrichment and notably varying N/O ratios, suggesting that material highly enriched ejected during the outburst has not yet mixed completely. The assumption on the shock completeness does not hold at the

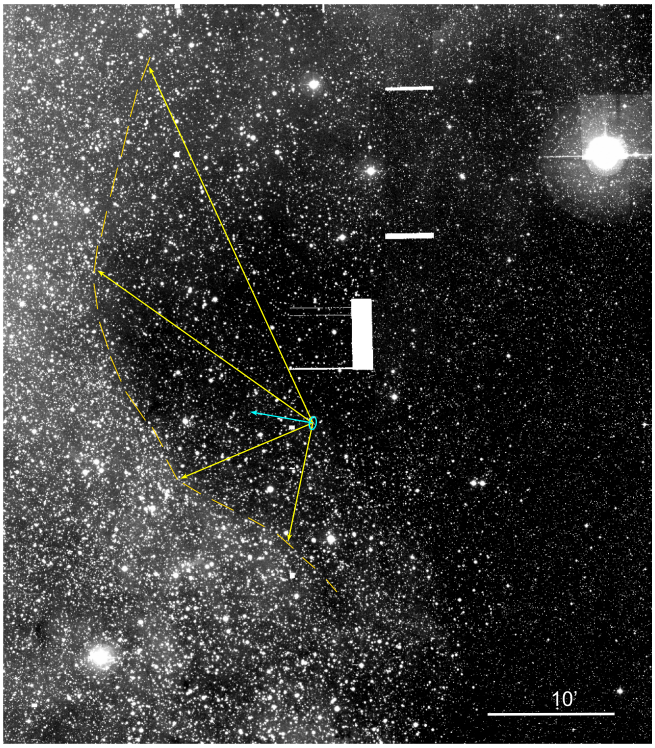

Figure 12. Large FoV IPHAS Hα+[N II] image around J210204. The cyan ellipse traces the bright [N II] ring of J210204 and the cyan arrow the direction of the [O III] bow shock. The yellow arrows and dashed line mark the location of the quasi circular arc described in the text.

bow shock, where abundances are uncertain, although they might be consistent with those of the ISM.

The bow shock is preceded by two additional arcs. These diffuse arcs of emission seem to trace the interaction of the ejecta of J210204 with the ISM, although they may also be the relics of previous events of mass ejection. To investigate recurrent interactions of mass loss processes from J210224 with the ISM, we have searched for large-scale diffuse emission features around J210204 in IPHAS mosaic images (Figure 12). These do not reveal any additional detached rings or arcs, but there is a quasi-semi-circular depression in the ISM material toward the northeast of J210204, more or less along the bow-shock direction (Figure 12). Although the presence of this structure is tantalizing, we note that the stars density inside this arc is notably smaller than on the arc, indicating that the origin of this arc can be associated most likely with varying ISM absorption rather than with recurrent episodes of mass ejection and their interaction with the ISM.

5. Conclusions

From the analysis of the time-resolved photometric and spectroscopic data of the central source of IPHASX J210204.7 +471015, it can be concluded that it hosts a binary system. The object can be classified as an old nova observed around a UX UMa system, i.e., a classical nova observed around a non-magnetic CV system observed at quiescence. The nebula shows evidences of nitrogen and oxygen enrichment, which is later diluted into the surrounding ISM by a fast ejecta resulting in a typical bow-shock structure. These are typical characteristics of a nova shell. Actually, the remnants of past ejections around CVs are scarcely detected (Ringwald et al. 1996; Gill & O'Brien 2000; Schmidtobreick et al. 2015; Tomov et al. 2015). A reclassification as a recurrent nova might be possible if the arc-like features 1.′5 and 2.′0 in front of the [O III] bow shock could be attributed to previous episodes of mass ejection from the nova.

M.A.G. acknowledges support of the grant AYA 2014-57280-P, cofunded with FEDER funds. L.S. acknowledges support from PAPIIT grant IA-101316 (Mexico). G.T. has been supported by grants PAPIIT IN108316 and CONACyT 166376. G.R.-L. acknowledges support from Universidad de Guadalajara, CONACyT, PRODEP, and SEP (Mexico). AA postdoctoral grant and some computational resources are from CONACyT 2015-CB/254132 and UNAM-DGAPA-PAPIIT-107215 projects. N.J.W. acknowledges an STFC Ernest Rutherford Fellowship.

This article is partially based upon observations carried out at the Observatorio Astronómico Nacional on the Sierra San Pedro Mártir (OAN SPM), Baja California, Mexico. We thank the daytime and night support staff at the OAN SPM for facilitating and helping obtain our observations. Some of the data presented here were obtained with ALFOSC, which is provided by the Instituto de Astrofísica de Andalucía (IAA) under a joint agreement with the University of Copenhagen and NOTSA. This article is based in part on observations made with the Gran Telescopio Canarias (GTC), installed in the Spanish Observatorio del Roque de los Muchachos of the Instituto de Astrofísica de Canarias, in the island of La Palma. This paper also makes use of data obtained as part of the INT Photometric Hα Survey of the Northern Galactic Plane (IPHAS: http://www.iphas.org) carried out at the Isaac Newton Telescope (INT). The INT is operated on the island of La Palma by the Isaac Newton Group in the Spanish Observatorio del Roque de los Muchachos of the Instituto de Astrofísica de Canarias. All IPHAS data are processed by the Cambridge Astronomical Survey Unit at the Institute of Astronomy in Cambridge. The band-merged DR2 catalog was assembled at the Centre for Astrophysics Research, University of Hertfordshire, supported by STFC grant ST/J001333/1.

Facilities: GTC(OSIRIS), ING:Newton(WFC), NOT(ALFOSC), OANSMP:0.8m (Mexman), OANSMP:2.1m (B&Ch).

ORCID iDs

Martín A. Guerrero https://orcid.org/0000-0002-7759-106X
Laurence Sabin https://orcid.org/0000-0003-0242-0044
Gagik Tovmassian https://orcid.org/0000-0002-2953-7528
Raul Michel https://orcid.org/0000-0003-1263-808X
Gerardo Ramos-Larios https://orcid.org/0000-0003-2653-4417

References

Asplund, M., Grevesse, N., Sauval, A. J., & Scott, P. 2009, ARA&A, 47, 481
Barentsen, G., Farnhill, H. J., Drew, J. E., et al. 2014, MNRAS, 444, 3230
Barentsen, G., et al. 2011, MNRAS, 415, 103
Beuermann, K., Stasiewski, U., & Schwope, A. D. 1992, A&A, 256, 433
Cannizzo, J. K. 1993, in Accretion Disks in Compact Stellar Systems, ed. C. J. Wheeler (Singapore: World Scientific), 6
Corradi, R. L. M., Valentini, M., Munari, U., et al. 2010, A&A, 509, A41
de Miguel, E., Patterson, J., Cejudo, D., et al. 2016, MNRAS, 457, 1447
Dhillon, V. S. 1996, ASSL, 208, 3
Drew, J. E., Gonzalez-Solares, E., Greimel, R., et al. 2014, MNRAS, 440, 2036
Drew, J. E., Greimel, R., Irwin, M. J., et al. 2005, MNRAS, 362, 753
Froebrich, D., Davis, C. J., Ioannidis, G., et al. 2011, MNRAS, 413, 480

Froebrich, D., Makin, S. V., Davis, C. J., et al. 2015, MNRAS, 454, 2586
Gaustad, J. E., McCullough, P. R., Rosing, W., & Van Buren, D. 2001, PASP, 113, 1326
Gehrz, R. D., Evans, A., & Woodward, C. E. 2014, ASP Conf. Ser. 490, Stella Novae: Past and Future Decades, ed. A. Woudt & V. A. R. M. Ribeiro, (San Francisco, CA: ASP), 227
Gill, C. D., & O'Brien, T. J. 2000, MNRAS, 314, 175
Gvaramadze, V. V., Kniazev, A. Y., Hamann, W.-R., et al. 2010, MNRAS, 403, 760
Hartigan, P., Raymond, J., & Hartmann, L. 1987, ApJ, 316, 323
Hernández, M. S., Zharikov, S., Neustroev, V., & Tovmassian, G. 2017, MNRAS, 470, 1960
José, J., & Hernanz, M. 1998, ApJ, 494, 680
Kalari, V. M., Vink, J. S., Drew, J. E., et al. 2015, MNRAS, 453, 1026
Lenz, P., & Breger, M. 2005, CoAst, 146, 53
Meyer, F., & Meyer-Hofmeister, E. 1982, A&A, 106, 34
Mineshige, S., & Osaki, Y. 1985, PASJ, 37, 1
Mohr-Smith, M., Drew, J. E., Barentsen, G., et al. 2015, MNRAS, 450, 3855
Neustroev, V. V., Suleimanov, V. F., Borisov, N. V., Belyakov, K. V., & Shearer, A. 2011, MNRAS, 410, 963
Nussbaumer, H., Schmid, H. M., Vogel, M., & Schild, H. 1988, A&A, 198, 179
Parker, Q. A., Acker, A., Frew, D. J., et al. 2006, MNRAS, 373, 79
Parker, Q. A., Bojičić, I. S., & Frew, D. J. 2016, JPhCS, 728, 032008
Parker, Q. A., Phillipps, S., Pierce, M. J., et al. 2005, MNRAS, 362, 689
Pretorius, M. L., & Knigge, C. 2008, MNRAS, 385, 1485
Raddi, R., Drew, J. E., Fabregat, J., et al. 2013, MNRAS, 430, 2169
Ringwald, F. A., Naylor, T., & Mukai, K. 1996, MNRAS, 281, 192
Roberts, D. H., Lehar, J., & Dreher, J. W. 1987, AJ, 93, 968
Sabin, L., Parker, Q. A., Contreras, M. E., et al. 2013, MNRAS, 431, 279
Sabin, L., Parker, Q. A., Corradi, R. L. M., et al. 2014, MNRAS, 443, 3388
Sahman, D. I., Dhillon, V. S., Knigge, C., & Marsh, T. R. 2015, MNRAS, 451, 2863
Schlegel, E. M., Honeycutt, R. K., & Kaitchuck, R. H. 1983, ApJS, 53, 397
Schmidtobreick, L., Shara, M., Tappert, C., Bayo, A., & Ederoclite, A. 2015, MNRAS, 449, 2215
Shara, M. M., Mizusawa, T., Wehinger, P., et al. 2012, ApJ, 758, 121
Stock, D. J., & Barlow, M. J. 2010, MNRAS, 409, 1429
Sutherland, R. S., & Dopita, M. A. 2017, ApJS, 229, 34
Tarasova, T. N. 2014, ARep, 58, 302
Tarasova, T. N. 2016, ARep, 60, 1052
Tomov, T., Swierczynski, E., Mikolajewski, M., & Ilkiewicz, K. 2015, A&A, 576, A119
Viironen, K., Greimel, R., Corradi, R. L. M., et al. 2009, A&A, 504, 291
Wesson, R., Barlow, M. J., Corradi, R. L. M., et al. 2008, ApJL, 688, L21
Witham, A. R., Knigge, C., Drew, J. E., et al. 2008, MNRAS, 384, 1277
Wright, N. J., Wesson, R., Drew, J. E., et al. 2014, MNRAS, 437, L1
Yang, M. T.-C., Chou, Y., Ngeow, C.-C., et al. 2017, PASP, 129, 094202